

THE PHOENIX DEEP SURVEY: THE 1.4 GHz MICROJANSKY CATALOG

A. M. HOPKINS,^{1,2} J. AFONSO,^{3,4} B. CHAN,⁵ L. E. CRAM,⁶ A. GEORGAKAKIS,⁷ AND B. MOBASHER⁸

Received 2002 September 27; accepted 2002 November 4

ABSTRACT

The initial Phoenix Deep Survey (PDS) observations with the Australia Telescope Compact Array have been supplemented by additional 1.4 GHz observations over the past few years. Here we present details of the construction of a new mosaic image covering an area of 4.56 deg², an investigation of the reliability of the source measurements, and the 1.4 GHz source counts for the compiled radio catalog. The mosaic achieves a 1 σ rms noise of 12 μ Jy at its most sensitive, and a homogeneous radio-selected catalog of over 2000 sources reaching flux densities as faint as 60 μ Jy has been compiled. The source parameter measurements are found to be consistent with the expected uncertainties from the image noise levels and the Gaussian source fitting procedure. A radio-selected sample avoids the complications of obscuration associated with optically selected samples, and by utilizing complementary PDS observations, including multicolor optical, near-infrared, and spectroscopic data, this radio catalog will be used in a detailed investigation of the evolution in star formation spanning the redshift range $0 < z < 1$. The homogeneity of the catalog ensures a consistent picture of galaxy evolution can be developed over the full cosmologically significant redshift range of interest. The 1.4 GHz mosaic image and the source catalog are available on the World Wide Web; or from the authors by request.

Key words: galaxies: evolution — galaxies: general — galaxies: starburst — radio continuum — surveys

1. INTRODUCTION

Exploration of star formation processes in galaxies through observations at radio wavelengths has developed rapidly in the past few years (Hopkins et al. 1998; Richards et al. 1998; Hopkins et al. 1999b; Richards 2000; Prandoni et al. 2001; Masci et al. 2001; Sadler et al. 2002; de Vries et al. 2002). By avoiding the problems associated with dust obscuration, dominant at optical wavelengths, radio data provide a valuable tool in understanding the full picture of star formation in galaxies. The evolution of these galaxies and the role of interactions and mergers in the population are still only partially understood.

The Phoenix Deep Survey (PDS) aims to catalog a large sample of *radio-selected* star-forming galaxies spanning the redshift range $0 < z < 1$. The PDS includes a 1.4 GHz survey made using the Australia Telescope Compact Array (ATCA) and covers a field a little more than 2° in diameter, selected to lie in a region of low optical obscuration and to be devoid of bright radio sources (Hopkins et al. 1998). To clarify our nomenclature, we use the acronym PDS to designate the survey as a whole, which includes multicolor optical photometry and spectroscopy, as well as the radio

imaging. The full 1.4 GHz ATCA mosaic itself, over which all the complementary multiwavelength observations have been conducted, is referred to as the Phoenix Deep Field (PDF). The PDF provides a large homogeneous sample of 1.4 GHz sources that, through the complementary multiwavelength observations of the PDS, is being used to investigate star-forming galaxies in the faint radio population. Existing analyses of the PDS (Afonso 2002; Afonso et al. 2001a, 2001b, 2001c, 1999; Georgakakis 1999; Georgakakis et al. 2000, 1999a, 1999b; Hopkins et al. 2000, 1999a, 1999b, 1998; Hopkins 1998; Mobasher, Afonso, & Cram 2001; Mobasher et al. 1999) have described the initial survey and catalogs and have initiated investigations into numerous aspects of the sample, including some implications for star formation processes in galaxies.

Recent ATCA observations have improved the sensitivity over a larger area within the PDF, allowing a larger radio catalog to be compiled and increasing the number of radio sources with optical counterparts. The new mosaic image is slightly larger than the original mosaic (Hopkins et al. 1998), and the catalogs constructed from it contain over 2000 identified radio sources. This corresponds to roughly a 30% increase over the number of sources available from the complete catalog used in the analysis of Hopkins et al. (1999b) and twice the number from the original catalog described by Hopkins et al. (1998). The additional source detections are a result of expanding the region over which we achieve the level of greatest sensitivity, comparable to that initially reported by Hopkins et al. (1999b). In § 2 of this paper we present the 1.4 GHz ATCA observations and summarize the image processing; § 3 describes the radio source measurements and their reliability; § 4 explains the compilation of the radio source catalogs; § 5 describes the construction of the 1.4 GHz source counts; § 6 presents the source-count results; § 7 provides a discussion of the similarities to and discrepancies with other source-count estimates; and § 8 summarizes our main results and conclusions.

¹ Department of Physics and Astronomy, University of Pittsburgh, 3941 O'Hara Street, Pittsburgh, PA 15260; ahopkins@phyast.pitt.edu.

² Hubble Fellow.

³ Centro de Astronomia e Astrofísica da Universidade de Lisboa, Observatório Astronómico de Lisboa, Tapada da Ajuda, PT-1349-018 Lisboa, Portugal.

⁴ Blackett Laboratory, Imperial College, Prince Consort Road, London SW7 2BW, UK.

⁵ School of Physics, University of Sydney, NSW 2006, Australia.

⁶ Australian Research Council, GPO Box 9880, Canberra, ACT 2601, Australia.

⁷ Institute of Astronomy and Astrophysics, National Observatory of Athens, I. Metaxa and Vas. Pavlou str., GR-15236 Athens, Greece.

⁸ Space Telescope Science Institute, 3700 San Martin Drive, Baltimore, MD 21218.

2. OBSERVATIONS

The PDF (Hopkins et al. 1999b, 1998; Hopkins 1998) covers a high-latitude region that is of low optical obscuration and devoid of bright radio sources. ATCA 1.4 GHz observations were made in 1994, 1997, 1999, 2000, and 2001 in the 6A, 6B, and 6C array configurations, accumulating a total of 523 hr of observing time. The initial 1994 ATCA observations (Hopkins et al. 1998; Hopkins 1998) consisted of 30 pointings on a hexagonal tessellation, resulting in a 2° diameter field centered on R.A. = $01^{\text{h}}14^{\text{m}}12^{\text{s}}.16$, decl. = $-45^\circ44'8''.0$ (J2000.0), with roughly uniform sensitivity of about $60 \mu\text{Jy}$ rms. This survey was supplemented from 1997 to 2001 by extensive observations of a further 19 pointings situated on a more finely spaced hexagonal grid, centered on R.A. = $01^{\text{h}}11^{\text{m}}13^{\text{s}}.0$, decl. = $-45^\circ45'00''$ (J2000.0). The locations of all pointing centers are given in Table 1.

Processing of the data was performed using the MIRIAD software package, following the steps detailed in Hopkins et al. (1998, 1999b). Some 1994 data were reprocessed to improve both the flagging of data affected by strong interference and the self-calibration of the brightest source in the field (a 115 mJy source toward the eastern edge of the mosaic). In the 1997–2001 observations some of the westernmost pointings showed side-lobe artifacts from a bright out-of-field source. For each affected pointing, these arti-

facts were removed as follows. First the object was imaged by applying an offset to the image center using MIRIAD's INVERT task, revealing a double component source. The MFCLEAN task was used to create a model for the source, and this model was subtracted from the flagged data using the task UVMODEL. Subsequent imaging of the affected fields (after MFCLEANing) showed no residual side-lobe artifacts from this source.

After using the task MFCLEAN to construct clean-component models for each pointing, the task RESTOR was used to make a clean image for each field, specifying a fixed restoring beam size of $6'' \times 12''$ (in the R.A. \times decl. sense) for all pointings. This was done in anticipation of the mosaicking step, to ensure that common sources in overlapping pointings were not represented by differently sized or oriented intensity distributions. The final mosaic was constructed from all 49 pointings, using the task LINMOS. The mosaic was then trimmed to remove the highest noise regions at the edges by masking out regions with an rms noise level greater than 0.25 mJy. This resulted in an image of 4781×4111 pixels (with a pixel scale of $2'' \text{ pixel}^{-1}$), shown in Figure 1. Figure 2 shows contours corresponding to the theoretical rms noise level for the mosaic (but see also Fig. 9 and the discussion in § 5), and a magnified view of the most sensitive portion of the mosaic is shown in Figure 3. The trimmed PDF mosaic image now covers an area of 4.56 deg^2 and reaches to a measured level of $12 \mu\text{Jy}$ rms noise in the most sensitive regions. With the addition of the more sensitive 1997–2001 data, the noise characteristics over the field are no longer uniform, as was the goal of the original 1994 project (Hopkins 1998). This is not so much a drawback as might be supposed however, as will be seen in the next section, describing source detection. Indeed, the combination of the deeper imaging with a shallower wide-field presents an opportunity to simultaneously explore properties of both the faintest radio sources and the brighter ones, from levels of about $50 \mu\text{Jy}$ to almost 50 mJy, although the sampling of the brightest sources will clearly still be sparser than the faintest.

Source confusion is not yet a concern for the survey, even at the flux density levels reached. From the number of sources detected and the area sampled (see § 4), even in the region of highest source surface density close to the flux density limits, there are still about 140 independent beam areas per source. This is sufficient to ensure that source confusion should not bias the survey, although observations to deeper levels at this resolution may start to be affected.

3. SOURCE DETECTION AND MEASUREMENT

The MIRIAD task SFIND (Hopkins et al. 2002) was used for detecting sources in the PDF mosaic. In an image such as the PDF mosaic, with a nonuniform mean and a continuously varying noise level, source detection by specifying a uniform threshold over the complete image is clearly not the correct approach. Calculation of locally determined rms noise levels over the image is necessary, and the SFIND task implements this by dividing the image into small square regions of a user-specified size within which the mean and rms noise level are estimated. These quantities are found by fitting a Gaussian to the pixel histogram in each region, after iterative σ -clipping to remove any bias from source pixels. The image is then “normalized” by subtracting the mean and dividing by the rms within each region, resulting

TABLE 1
MOSAIC POINTINGS OBSERVED WITH ATCA

R.A. (J2000.0)	Decl. (J2000.0)	R.A. (J2000.0)	Decl. (J2000.0)
1994		1997–2001	
01 09 13.589	-45 44 01.41	01 08 44.200	-45 30 00.00
01 10 13.123	-45 59 02.70	01 08 44.200	-45 45 00.00
01 10 13.480	-45 29 02.70	01 08 44.200	-46 00 00.00
01 11 12.651	-46 14 04.00	01 09 58.600	-45 22 30.00
01 11 13.016	-45 44 04.01	01 09 58.600	-45 37 30.00
01 11 13.374	-45 14 04.01	01 09 58.600	-45 52 30.00
01 12 12.173	-46 29 05.32	01 09 58.600	-46 07 30.00
01 12 12.546	-45 59 05.33	01 11 13.000	-45 15 00.00
01 12 12.912	-45 29 05.33	01 11 13.000	-45 30 00.00
01 12 13.272	-44 59 05.34	01 11 13.000	-45 45 00.00
01 13 12.070	-46 14 06.66	01 11 13.000	-46 00 00.00
01 13 12.444	-45 44 06.67	01 11 13.000	-46 15 00.00
01 13 12.812	-45 14 06.68	01 12 27.400	-45 22 30.00
01 14 11.587	-46 29 08.02	01 12 27.400	-45 37 30.00
01 14 11.970	-45 59 08.03	01 12 27.400	-45 52 30.00
01 14 12.346	-45 29 08.03	01 12 27.400	-46 07 30.00
01 14 12.716	-44 59 08.04	01 13 41.800	-45 30 00.00
01 15 11.490	-46 14 09.40	01 13 41.800	-45 45 00.00
01 15 11.874	-45 44 09.41	01 13 41.800	-46 00 00.00
01 15 12.252	-45 14 09.41		
01 16 11.003	-46 29 10.79		
01 16 11.396	-45 59 10.80		
01 16 11.782	-45 29 10.80		
01 16 12.162	-44 59 10.81		
01 17 10.911	-46 14 12.21		
01 17 11.306	-45 44 12.21		
01 17 11.694	-45 14 12.22		
01 18 10.824	-45 59 13.64		
01 18 11.220	-45 29 13.65		
01 19 10.739	-45 44 15.09		

NOTE.—Units of right ascension are hours, minutes, and seconds, and units of declination are degrees, arcminutes, and arcseconds.

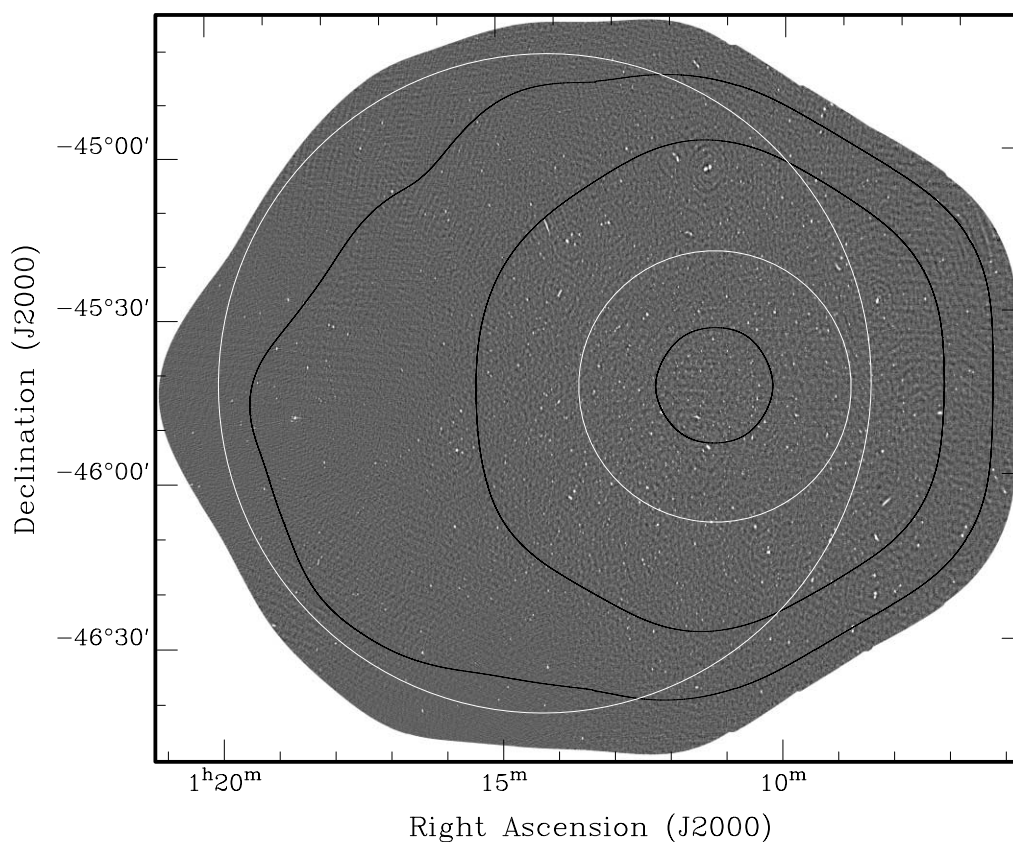


FIG. 1.—Complete Phoenix Deep Field mosaic. The gray-scale image has been trimmed at the $250 \mu\text{Jy}$ rms contour. The large white circle shows the 2° diameter region of the original PDF (Hopkins et al. 1998). The small white circle corresponds to the $25 \mu\text{Jy}$ rms contour as measured in an earlier mosaic, which delimited the $50'$ diameter deep subregion described in Hopkins et al. (1999b). (The $25 \mu\text{Jy}$ rms contour of the current mosaic is not shown here but covers a larger area; see Fig. 2.) The black contours mark the theoretical 10, 30, and $90 \mu\text{Jy}$ rms levels of this mosaic, emphasizing the high sensitivity over a region roughly 2° in diameter. This image has been normalized by subtracting locally determined means and dividing by locally determined rms noise values, to emphasize the sources rather than the noise characteristics. Note the uniformity of the background once the varying noise level has been accounted for and the apparent predominance of sources in the regions corresponding to the greatest sensitivity of the survey.

in an image where pixel values are effectively specified in units of σ , the local rms noise level. This normalized image can be used for defining a threshold for source-detection, specifying which pixels to use in measuring the source

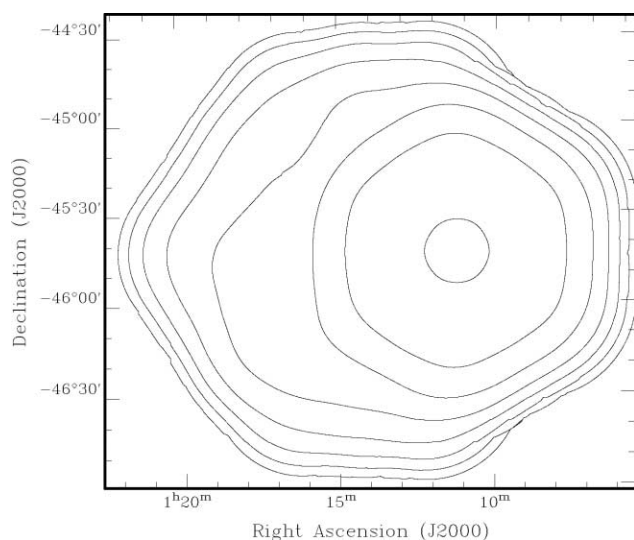


FIG. 2.—Contours showing the theoretical rms noise level over the full 1.4 GHz mosaic, ranging from $10 \mu\text{Jy}$ (inner circle) to 1.28 mJy , in steps of factors of 2.

parameters, which is then performed using the original image. The “normalized” PDF mosaic (constructed using regions of 100×100 pixels for estimating the noise characteristics) is shown in Figure 1.

By normalizing the image before performing the thresholding for the source detection, the nonuniform noise level of the original mosaic is no longer an issue when constructing a source catalog. Deciding how to choose the threshold is the next important question. Traditionally, levels such as 5σ or even 7σ have been chosen to ensure a minimum number of falsely detected sources. Such strict thresholds bring some level of confidence in the detected sources at the expense of overlooking many real fainter sources. Lower thresholds, on the other hand, detect many more sources but with a higher probability that any given source is spurious. One way of addressing this issue is to use a statistical technique called the false discovery rate (FDR), which assigns a threshold based on an acceptable rate of false detections (Hopkins et al. 2002; Miller et al. 2001). As described in detail by those authors, an arbitrarily chosen significance threshold such as 5σ can fix the total number of false detections in an image, (which will depend for example on the image size and sampling), independently of the number of real sources detected. The FDR method, in contrast, controls what is perhaps a more relevant quantity, the average fraction of false discoveries over the total number of

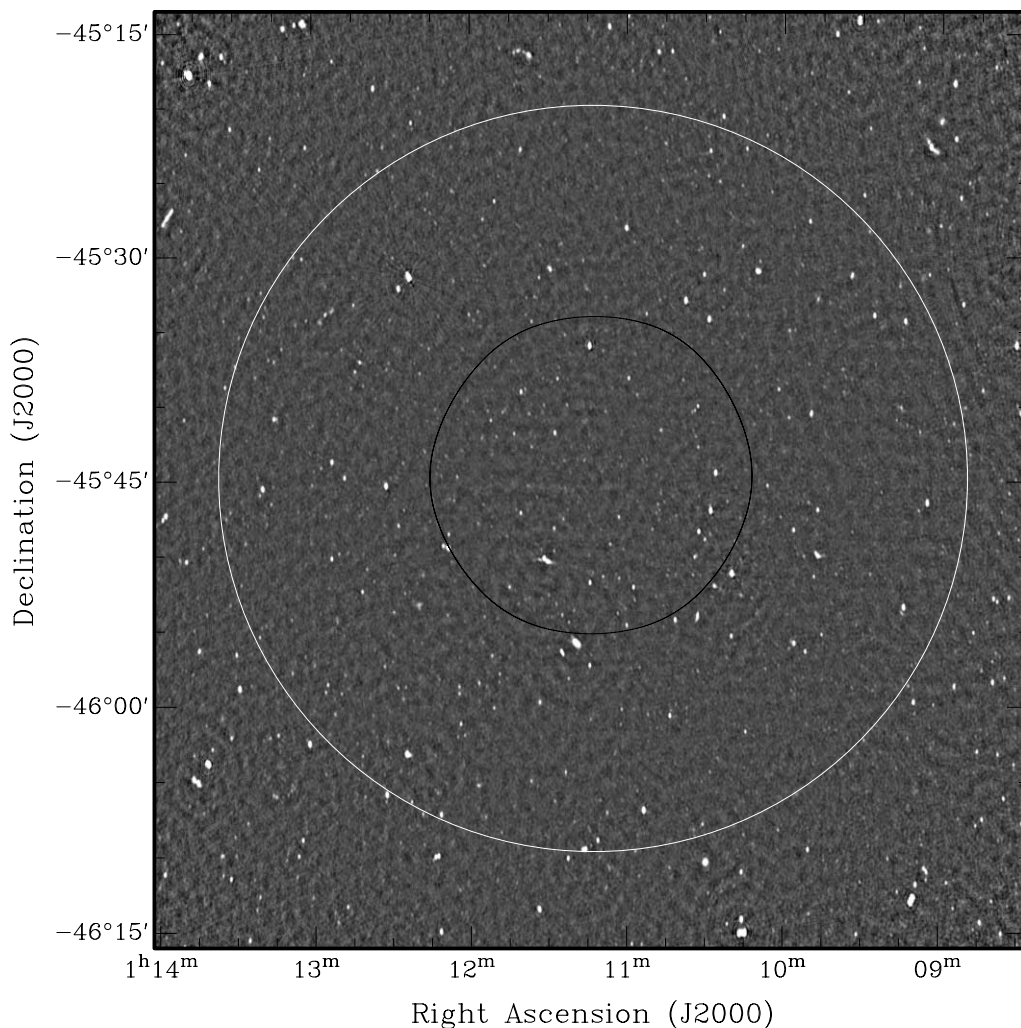


FIG. 3.—Magnified view of a $63' \times 63'$ region centered on the most sensitive portion of the new PDF mosaic, showing a selection of sources in more detail. Circles and contour as in Fig. 1.

discoveries (Miller et al. 2001). The FDR method achieves this by adapting the threshold to the data (image background plus sources) being analyzed. By specifying that, say, 10% of the detected sources are allowed to be false detections, a specific threshold would be defined for a given image that would ensure no more than 10% of the detections would be false. There is a further subtlety here deriving from the relation of astronomical sources to the source pixels comprising them in an image, since it is actually the source pixels whose false discovery rate is governed by the FDR technique. This is explored in detail by Hopkins et al. (2002), who conclude that, in general, the false discovery rate specified for the pixels will correspond fairly closely to that for the astronomical sources of interest. Deviations of the image background from true Gaussian noise though, as may occur due to residual imaging artifacts for example, may act to increase the number of false detections somewhat, although this is true of any thresholding technique.

The reliability of the source detection for the PDF using SFIND was investigated by taking advantage of the overlapping nature of the many pointings used to construct the mosaic. Several overlapping fields were first corrected for the attenuation of the primary beam sensi-

tivity, after which source detection was performed independently on each. The task SFIND was used for the source detection, specifying a false discovery rate of 10%. Common sources between each pair of fields were identified by positional matching, assuming that a positional offset of less than $2''$ indicated a common source. The measurements of the source parameters (positions and flux densities) for common sources were compared to ascertain their reliability. In Figure 4 the positional uncertainties are shown. The histograms in Figure 4 reflect the fact that the synthesized beam size is twice as large in declination as in right ascension and indicate that the relative rms positional uncertainty from the SFIND measurements is less than about $0''.5$.

To investigate the reliability of the flux density measurements, the uncertainties in the measurements need to first be established. The relative error in the integrated flux density I for a source was estimated from

$$\frac{\sigma_I}{I} = \sqrt{\frac{\mu_{\text{image}}^2}{I^2} + \frac{\mu_{\text{fit}}^2}{I^2}}, \quad (1)$$

where μ_{image} is the uncertainty due to the rms noise in the image, and μ_{fit} is the uncertainty in the Gaussian fitting.

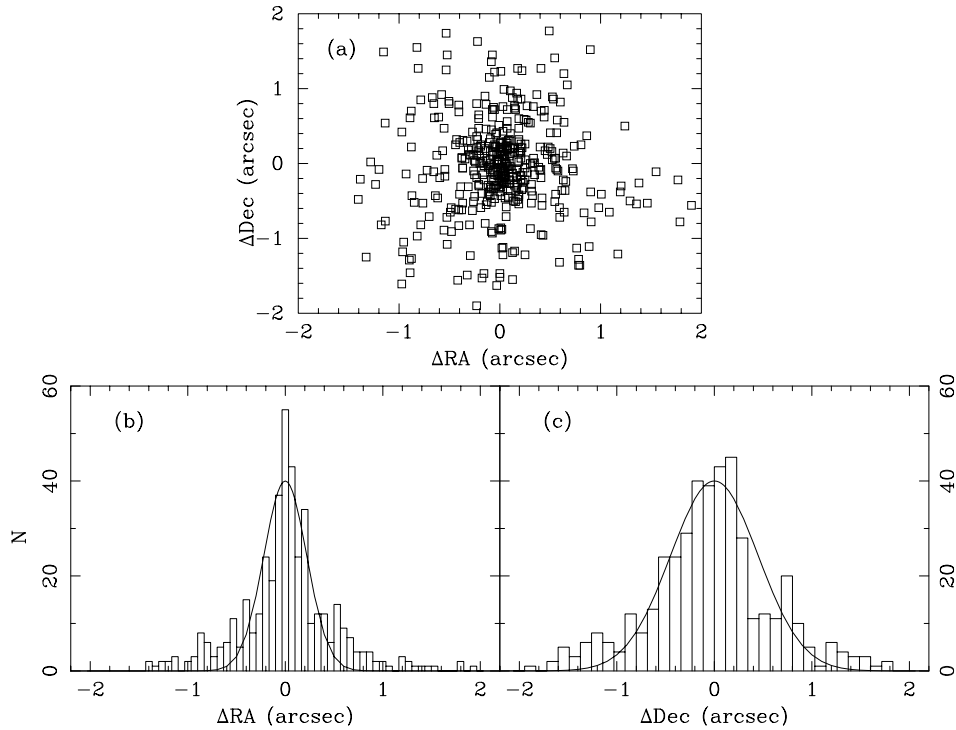


FIG. 4.—(a) Relative positional offsets in right ascension and declination for common objects detected independently in overlapping fields. Common sources were identified as those having positions separated by less than $2''$, and this is reflected in the limits of the uncertainties shown here. (b)–(c) Histograms of relative positional offsets for common objects. The solid lines are Gaussian fits to the histograms and indicate the magnitude of the relative positional uncertainties. For right ascension, the Gaussian shown has $\sigma = 0''.22$, for declination it has $\sigma = 0''.45$. These values are a result of the fact that the synthesized beam shape is twice as wide in declination as in right ascension. The presence of the outliers above the Gaussian fits are due to the presence of both intrinsically non-Gaussian sources as well as falsely detected pixels that skew the measurements for some objects. In general the rms positional uncertainties from the SFIND measurements should be better than about $0''.5$.

From Windhorst, van Heerde, & Katgert (1984),

$$\frac{\mu_{\text{image}}}{I} = \sqrt{\frac{\sigma^2}{S^2} + C_f^2 + C_p^2}, \quad (2)$$

where σ is the rms noise at the location of the source, S is the peak flux density of the source, C_f is the relative error in the absolute flux calibration, and C_p is the relative flux error introduced due to pointing errors of the individual telescope dishes. The latter two terms combined are of the order of 1% ($C_f^2 + C_p^2 = 0.01^2$), and this value has been used for subsequent calculations. The rms noise in the image is correlated over the synthesized beam area, and from equation (42) of Condon (1997) the relative uncertainty from the fitting is taken to be

$$\frac{\mu_{\text{fit}}^2}{I^2} = \frac{\mu_S^2}{S^2} + \left(\frac{\theta_B \theta_b}{\theta_M \theta_m}\right) \left[\frac{\mu_M^2}{\theta_M^2} + \frac{\mu_m^2}{\theta_m^2}\right], \quad (3)$$

where $\theta_B \theta_b$, the product of the synthesized beam major and minor axis full width at half maxima, is used in place of Condon's θ_N^2 . (Condon assumes a circular Gaussian shape for the smoothing, corresponding to the area over which the noise is correlated, whereas we have an elliptical Gaussian shape.) The uncertainties μ_S , μ_M , and μ_m are those due to the fitting in the peak flux density S , major axis θ_M , and minor axis θ_m , respectively. These are approximated by Condon's equation (21), $\mu_X/X^2 \approx 2/\rho_X^2$, where ρ_X , the signal-to-noise ratio (S/N) of the fit, is parameter dependent, as given by Condon's

equation (41),

$$\rho^2 = \frac{\theta_M \theta_m}{4\theta_B \theta_b} \left[1 + \left(\frac{\theta_B}{\theta_M}\right)^2\right]^{\alpha_M} \left[1 + \left(\frac{\theta_b}{\theta_m}\right)^2\right]^{\alpha_m} \frac{S^2}{\sigma^2}, \quad (4)$$

which we have again modified, using θ_B and θ_b in place of Condon's θ_N in the appropriate places. The parameter dependence enters through the exponents α_M and α_m , which, again following Condon (1997), we take to be $\alpha_M = \alpha_m = 1.5$ for calculating μ_S^2/S^2 , $\alpha_M = 2.5$ and $\alpha_m = 0.5$ for μ_M^2/θ_M^2 , and $\alpha_M = 0.5$, $\alpha_m = 2.5$ for μ_m^2/θ_m^2 . For point sources ($\theta_M = \theta_B$, $\theta_m = \theta_b$, $I = S$) the total relative uncertainty in the integrated flux density reduces to

$$\frac{\sigma_I}{I} = \sqrt{2.5 \frac{\sigma^2}{I^2} + 0.01^2} \quad (5)$$

(compare with eq. [9] of Rengelink et al. 1997).

With the value of σ_I/I now determined for each source, we can explore the flux density measurements of common sources detected in independent observations. For each pair of detections of a common source, the combined uncertainty is simply the quadrature sum of the individual relative uncertainties. The S/N for each pair is then taken to be the inverse of this combined uncertainty. The ratio of integrated flux density measurements I_1/I_2 is shown plotted as a function of the combined S/N in Figure 5. The uncertainties in the flux density ratios (the inverse of the combined S/N) are shown as the solid and dashed lines, indicating the 1σ and 3σ uncertainty levels, respectively. There are a few outliers

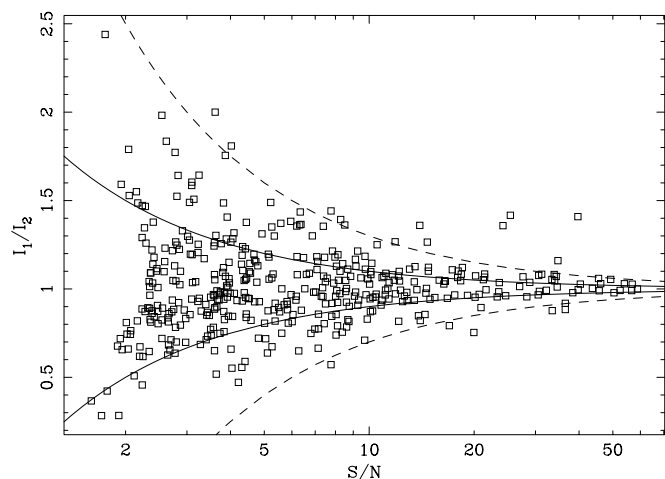


FIG. 5.—Integrated flux density ratios as a function of the combined S/N for common sources measured in independent observations. The solid and dashed lines indicate the 1σ and 3σ uncertainties expected from eq. (1).

in this diagram that do not follow the expected uncertainty distribution. These will be examined further below.

A second flux density measurement comparison was done following the method used by Windhorst et al. (1984). By subtracting unity from the flux ratios of independent measurements for common objects, then dividing by the combined rms for the measurements, they aimed to construct a normally distributed statistic, $A = (I_1/I_2 - 1)/(\sigma_1^2 + \sigma_2^2)^{1/2}$. A histogram of this statistic for all common objects in a pair of overlapping fields can be compared with a Gaussian of zero mean and unit rms to establish the reliability of the flux density measurements (Windhorst et al. 1984, their Figs. 4e and 4f). This particular statistic, though, is not sym-

metrical about zero when the flux density measurements are switched, suggesting that there may be some skew in the distribution, rather than truly being normally distributed. To avoid this problem, the following statistic was used:

$$A_1 = \frac{(I_1 - I_2)}{\sqrt{\sigma_1^2 + \sigma_2^2(I_1 + I_2)/2}}. \quad (6)$$

A related statistic, giving very similar results, is

$$A_2 = \frac{(I_1 - I_2)}{(I_1 \times I_2) \sqrt{(\sigma_1/I_1)^2 + (\sigma_2/I_2)^2}}. \quad (7)$$

Histograms of A_1 are shown in Figure 6 for six pairs of fields, the central field in the hexagonal tessellation of the 1997–2001 observations matched with each of the surrounding six fields (see Table 1). The majority of sources seem to be consistent with the expected uncertainties, and the few outliers are consistent with the FDR threshold used. Less than 10% of the sources detected are seen as outliers here, as expected from the FDR threshold defined by allowing up to 10% false detections. The outliers found by Windhorst et al. (1984) were variable or extended sources whose flux density comparisons would not be expected to follow such a distribution. As the fields compared here were all observed at the same time, variable sources should not make a significant contribution. Extended, intrinsically non-Gaussian sources may account for a small fraction of these outliers, but the majority of the detected sources are not significantly extended and the Gaussian model should be reasonable. Visual inspection of many of the objects responsible for the outliers in Figures 5 and 6 suggest that almost all of them are explained by variations in the Gaussian fits due

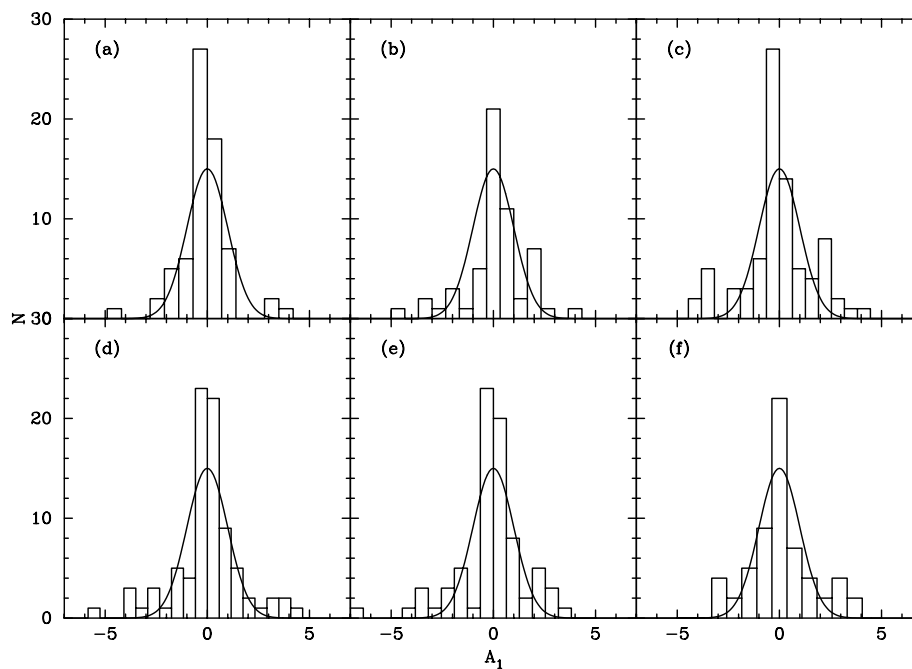


FIG. 6.—Histograms showing normalized flux ratios, A_1 , given by eq. (6). Each histogram contains data for common sources between a given pair of fields, for six pairs examined. The Gaussians are not fits to the data but are shown to guide the eye. They have zero mean, unit rms, and peak amplitude of 15. The histogram bin widths were chosen to produce histograms of an appropriate amplitude for convenience of comparison. The majority of sources seem to be consistent with the expected uncertainties, and the small number of outliers in each field are consistent with the FDR threshold used.

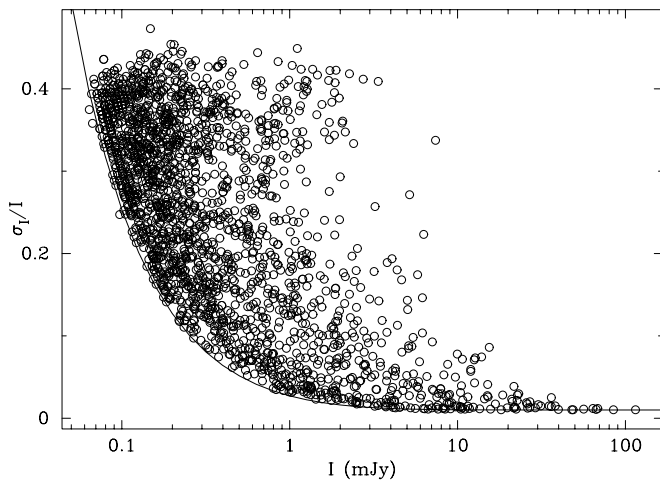


FIG. 7.—Relative flux density uncertainties as a function of integrated flux density for the complete PDF catalog. The solid line shows the expected locus for point sources as given by eq. (5), for a region of rms noise background of $16 \mu\text{Jy}$. For bright sources, well above the noise level, the second term in eq. (5) dominates.

to the presence of falsely detected pixels included with the source pixels during the source measurement.

The source measurements, both position and flux density, seem internally consistent within the expected uncertainties. To explore the actual values of the uncertainties, SFIND was used to compile a catalog for the full PDF mosaic, again using an FDR threshold of 10%, giving a total of 2058 sources (see § 4). The relative uncertainties in the integrated flux density are shown in Figure 7, with a line indicating the expected uncertainties for point sources as given by equation (5), using a background rms noise level of $16 \mu\text{Jy}$. This assumed background level is only significant for the fainter sources, since at high S/N the second term in equation (5) dominates. The value of the assumed background level selected corresponds to the local rms noise level in the vicinity of the faintest detected sources.

4. CATALOG CONSTRUCTION

The catalog for the full PDF was compiled using SFIND with a 10% FDR threshold, resulting in 2090 sources. The source parameters recorded in the catalog are the source position, peak and integrated flux densities and uncertainties, source size and orientation (major and minor axis full width at half maxima, and position angle measured east of north), and the rms noise level in the image at the location of the source. The source sizes have not been deconvolved from the synthesized beam size, so sources of $12'' \times 6''$ are point sources. Part of the SFIND algorithm includes checking for source parameters indicating an object smaller than the synthesized beam size. Following the suggestion of Condon (1997), such sources are automatically refitted assuming they are point sources (i.e., size and position angle are taken to be those of the synthesized beam, and only position and flux density are derived) and retained if the fitting converges.

A number of objects clearly associated with imaging artifacts, determined through subsequent visual inspection of all the cataloged sources, were removed, leaving 2058 sources in the final primary PDF catalog. Spurious objects

will still remain in this catalog, up to 10% of the total sources as given by the FDR threshold used (Hopkins et al. 2002). Visual inspection of most of the few extended or complex sources in the image confirm that many of these are poorly represented by the automated detection process, usually being detected as several overlapping Gaussian sources. We have not altered the detection parameters for these at all, primarily since the total number of such objects is small and the few poorly estimated parameters will not adversely affect the global properties of the catalog. Maintaining the easily quantified characteristics of the catalog construction is also important for understanding the relative numbers of false detections, for example, while still ensuring such complex sources remain in the catalog in some form for subsequent analysis. A histogram showing the complete distribution of integrated flux densities is shown in Figure 8, and Table 2 shows a short extract from the primary PDF catalog. In Table 2 and in the source-count analysis below we adopt the notation S_{peak} and S_{int} rather than S and I , since S is commonly used in diagrams of source counts to indicate the integrated flux density. We follow that convention here in our subsequent figures.

In addition to the primary PDF catalog, we also independently compiled a separate catalog of sources in a region of $33' \times 33'$ (1000×1000 pixels) centered on the most sensitive portion of the survey. The actual flux density threshold derived for this region happens to be slightly lower than that for the primary PDF catalog, even though a 10% FDR threshold was specified for each. This emphasizes a somewhat nonintuitive feature of FDR thresholds, a result of their adaptive nature. It turns out that, simply because of the lower noise level, the most sensitive region of the survey has a higher surface density of detectable sources than the survey as a whole. So to maintain the requested false discovery rate of 10% a lower threshold is required (giving more detections). The full survey area, however, even though it contains this region within it, has a lower average surface density of sources, and enough sources to reach a 10% false detection rate are detected at a higher threshold. This can also be understood by considering the effects of differing source surface densities on diagrams like Figure 1 of Hopkins et al. (2002). The main result of this adaptive effect of the FDR threshold for the current analysis is that the independent

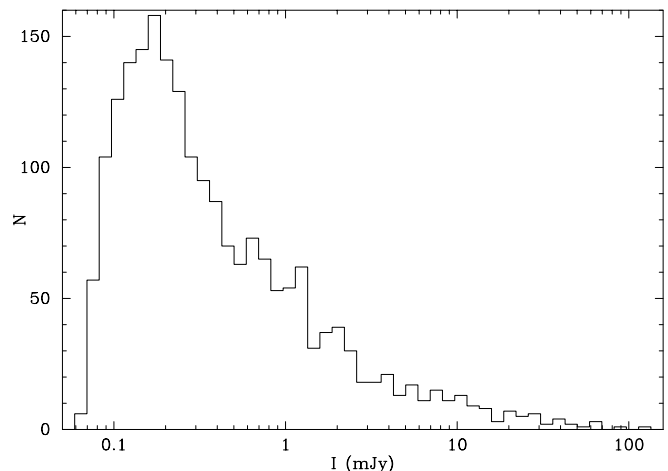


FIG. 8.—Histogram of integrated flux densities for the sources detected in the primary PDF catalog.

TABLE 2
EXTRACT FROM THE PDF CATALOG

R.A. (J2000.0)	Decl. (J2000.0)	S_{peak} (mJy)	S_{int} (mJy)	θ_{major} (arcsec)	θ_{minor} (arcsec)	P.A. (deg)	σ (mJy)
1 08 26.641	-45 42 27.38	0.524 ± 0.029	0.524 ± 0.040	12.0	6.0	0.0	0.020
1 08 26.778	-45 30 03.85	0.158 ± 0.041	0.158 ± 0.058	12.0	6.0	0.0	0.029
1 08 27.499	-46 07 42.57	0.433 ± 0.036	0.543 ± 0.062	13.1	6.9	2.9	0.025
1 08 27.760	-45 54 11.86	0.103 ± 0.028	0.155 ± 0.055	13.4	8.1	2.5	0.019
1 08 27.979	-45 43 24.75	0.330 ± 0.028	0.330 ± 0.040	12.0	6.0	0.0	0.020
1 08 28.928	-46 15 45.24	0.171 ± 0.048	0.171 ± 0.068	12.0	6.0	0.0	0.034
1 08 28.932	-45 40 21.55	1.122 ± 0.031	1.343 ± 0.049	13.1	6.6	5.1	0.020
1 08 29.137	-45 32 39.39	0.368 ± 0.041	0.368 ± 0.058	12.0	6.0	0.0	0.029
1 08 29.367	-46 11 43.36	0.155 ± 0.045	0.222 ± 0.086	14.9	6.9	8.5	0.031
1 08 29.467	-45 48 48.49	0.224 ± 0.027	0.224 ± 0.038	12.0	6.0	0.0	0.019
1 08 30.033	-45 11 37.96	0.284 ± 0.054	0.428 ± 0.107	15.1	7.2	-4.9	0.037
1 08 30.244	-45 39 52.15	0.140 ± 0.031	0.251 ± 0.070	16.5	7.8	11.2	0.021
1 08 30.249	-45 13 20.37	0.599 ± 0.053	0.866 ± 0.101	13.9	7.5	-3.1	0.036
1 08 30.433	-45 58 46.39	0.114 ± 0.029	0.185 ± 0.062	14.2	8.2	8.2	0.020
1 08 30.586	-45 48 01.06	0.164 ± 0.027	0.164 ± 0.038	12.0	6.0	0.0	0.019
1 08 30.694	-45 44 48.11	0.169 ± 0.028	0.169 ± 0.040	12.0	6.0	0.0	0.020
1 08 30.711	-46 03 47.59	0.257 ± 0.031	0.351 ± 0.056	12.6	7.8	-0.6	0.021
1 08 30.719	-46 04 04.88	0.124 ± 0.030	0.124 ± 0.042	12.0	6.0	0.0	0.021
1 08 30.753	-45 35 49.28	9.502 ± 0.101	11.038 ± 0.123	12.7	6.6	-0.7	0.024
1 08 32.847	-46 13 11.18	0.168 ± 0.044	0.168 ± 0.062	12.0	6.0	0.0	0.031
1 08 33.018	-45 52 40.20	0.599 ± 0.028	0.782 ± 0.049	13.0	7.3	-1.8	0.019
1 08 33.159	-45 45 43.37	0.223 ± 0.029	0.288 ± 0.050	12.1	7.7	10.1	0.020
1 08 33.247	-45 06 21.28	4.351 ± 0.128	5.731 ± 0.221	13.5	7.0	-5.7	0.083
1 08 34.528	-45 58 02.12	0.310 ± 0.028	0.397 ± 0.048	13.2	7.0	1.4	0.019
1 08 34.541	-46 06 03.47	0.660 ± 0.029	0.660 ± 0.041	12.0	6.0	0.0	0.020
1 08 34.788	-46 16 18.63	0.299 ± 0.043	0.431 ± 0.081	14.1	7.3	-3.3	0.029
1 08 34.846	-45 54 46.14	0.100 ± 0.025	0.207 ± 0.064	15.5	9.6	23.8	0.017
1 08 35.179	-45 16 46.28	0.213 ± 0.041	0.213 ± 0.058	12.0	6.0	0.0	0.029
1 08 35.301	-46 15 01.38	0.637 ± 0.043	0.867 ± 0.077	14.0	7.0	-0.2	0.029
1 08 35.959	-45 46 59.15	0.116 ± 0.026	0.157 ± 0.047	12.3	8.0	7.2	0.018

catalog from the deepest region contains fainter sources than the primary source catalog for the PDF, as well as a number of other sources absent in the primary catalog. This also explains why an rms noise level of 16 μJy is seen in Figure 7 rather than the lowest noise level in the image.

The effect of choosing different FDR thresholds (say 5% or 1%) is, as expected, to reduce the numbers of faint sources detected, while still detecting the same high S/N objects. This suggests that the majority of the falsely detected sources lie at flux densities close to the survey limit, which is as expected for any thresholding technique. As discussed further below, the primary effect of this will be to increase the uncertainties on the estimate of the source counts at the faintest flux densities. It is important to note that the actual fraction of falsely detected sources is constrained to be *at most* the FDR fraction specified (although the actual fraction cannot be known a priori), and can be significantly less in some cases, as seen in the simulations of Hopkins et al. (2002). So the optimistic viewpoint would be that there is *less* than a 10% false detection rate in a 10% FDR threshold catalog. The effect of choosing a very conservative threshold (1%, say) is to increase the reliability of the detected sources at the expense of missing many real, fainter sources. Since a primary goal of the PDS is to fully exploit the sensitivity of the deep 1.4 GHz survey, the more liberal FDR threshold of 10% was selected to maximize the number of sources close to the survey threshold while maintaining an acceptable rate of false detections.

Alternative catalogs can (and should) also be constructed from the PDF by using different thresholds (either FDR-determined or more traditionally by specifying some σ -related threshold), or different algorithms. The possibility of eventually seeing a robust, consistent source list constructed from independently compiled catalogs is one reason we have chosen to make the PDF image public.

5. SOURCE COUNTS

With the catalogs now available we proceed to construct the 1.4 GHz differential source counts for the PDF, and to compare them with earlier source-count estimates. We proceed in a similar fashion to that described in Hopkins et al. (1999b, 1998). To account for extended sources with integrated flux densities above the catalog limits but missed by the detection algorithm as a result of having peak flux densities below the detection limit, a resolution correction was applied using the same method and form as in Hopkins et al. (1998). A weighting correction is also applied to account for the varying areas over which sources of different flux densities could be detected. Detailed descriptions of the weighting and resolution corrections, and their necessity, are given elsewhere (Hopkins et al. 1998; Windhorst et al. 1984; Condon, Condon, & Hazard 1982; Oosterbaan 1978; Katgert et al. 1973).

Since one primary goal of constructing the catalogs is to identify a large population of radio-selected star-forming galaxies based on complementary optical photometry and

spectroscopy, allowing a certain fraction of falsely detected sources to enter the catalog is acceptable, as false sources may be less likely to have optical counterparts (although this is a strong function of the depth of the optical survey being compared with). For the purposes of constructing source counts, though, the presence of false sources may bias the resulting counts high. We have made no attempt to remove such sources from the catalog prior to constructing the source counts, however, as it is not a priori known which sources are false. Since it is likely that the majority of the false sources will occur at the faintest flux density levels, where the uncertainties in the resolution and weighting corrections will be largest, the most likely outcome is that the uncertainty in the faintest few source-count bins will be a little larger than estimated.

In calculating the weighting correction, the effective area over which each source could be detected is determined. The effective area for the whole PDF is shown in Figure 9 as a function of the rms noise level in the mosaic. The fraction of the total survey area is derived from both the theoretical noise image, constructed using the MIRIAD task LINMOS, and as derived from measurements made in the mosaic image itself. The theoretical rms noise level in the image reaches below $10 \mu\text{Jy}$, consistent with the earlier results of Hopkins et al. (1999b). The source detection, though, makes use of the measured image noise level, and it is these values which need to be used in determining the effective area over which each source could be detected. In constructing the source counts for the deep independent region, the weighting corrections derived for a given rms noise level are smaller than for the whole PDF. This is because the deep independent region has a more uniform noise level over a smaller total extent.

It should be noted that since we do not make any attempt to combine the components of multiple component sources, the source counts constructed from such a “component catalog” (rather than a “source catalog”) may be somewhat biased. The extent of this effect will be flux density dependent and (as discussed in § 7) of the order of about 10% around 1 mJy. With the majority of the PDF sources being fainter than 1 mJy, and with the decreasing contribution of

multiple-component AGN type sources at submillijansky levels, the extent of any such bias in this regime is expected to be small. Above about 1 mJy, though, such an effect may contribute to the source counts constructed herein.

A further issue regarding possible sources of uncertainty in constructing the source counts is related to objects close to the detection limit with large $S_{\text{int}}/S_{\text{peak}}$. These objects will have a large weighting correction by virtue of only being detectable over a small effective area. With a large integrated flux density that correction translates into a disproportionate contribution to a flux density bin where the majority of sources contribute fairly low weights. This can result in a source-count bin with both a comparatively high count and a large uncertainty. If many bins are affected by objects like this the source counts can appear both biased upward and highly variable over a small range in flux density. Investigation of the measured sizes of low-S/N objects ($S_{\text{peak}}/\sigma < 5$) reveals that they have larger median sizes than higher S/N sources at corresponding flux densities, suggesting that their sizes and hence integrated flux densities are overestimated. To avoid such biases from these sources, objects in the primary PDF catalog with $S_{\text{int}}/S_{\text{peak}} > 2.5$ and $S_{\text{peak}}/\sigma < 5$ are deemed to contribute to the flux density bin corresponding to their peak flux density (as though they were point sources) when constructing the source counts, rather than that for their overestimated integrated flux density. Similarly, for the deep independent catalog with a different threshold level, limits of $S_{\text{int}}/S_{\text{peak}} > 1.6$ and $S_{\text{peak}}/\sigma < 5.5$ were established to eliminate these artifacts. The number of such sources is 73 out of 2058 for the primary catalog and 71 out of 491 for the deep independent catalog (where a larger fraction of sources are closer to the survey limit), so there should be little effect on the source counts themselves apart from avoiding this type of artifact. It was found that omitting these sources entirely (on the tentative assumption that such objects might be false sources) had the effect only of marginally lowering the derived source counts in the faintest flux density bin for each catalog. They have been retained in the source counts presented here.

With this concern addressed, we now construct a resolution correction (r), as given in Hopkins et al. (1998), and a weighting correction ($w = T/D$, where T is the total survey area and D is the effective area over which the source could be detected) for each source, based on that source’s integrated and peak flux densities, respectively. Each source thus contributes a number of effective sources, $N_{\text{eff}} = rw$, to the flux density bin in the source counts in which its integrated flux density falls. Uncertainties on this value in each source-count bin are the rms counting errors, $[\sum_i (r_i w_i)^2]^{0.5}$. The width of the flux density bins are chosen to include a minimum number of actual sources per bin, apart from the brightest bin. The minimum number chosen was 150 sources per bin for the primary catalog for whole mosaic image and 60 for the deep independent catalog. Ensuring such large numbers of actual sources are present in each bin should minimize fluctuations in the resulting source counts. The final source counts are constructed by dividing these total effective numbers of sources per bin by the total survey area and the bin width, to give the number of sources per unit area per unit flux density, and then normalizing by the Euclidean slope of $S^{-2.5}$. The reason for the normalization step is historical in origin, relating to the early cosmological goals of studying radio source counts, and the greater ease of distinguishing different forms of evolution after such

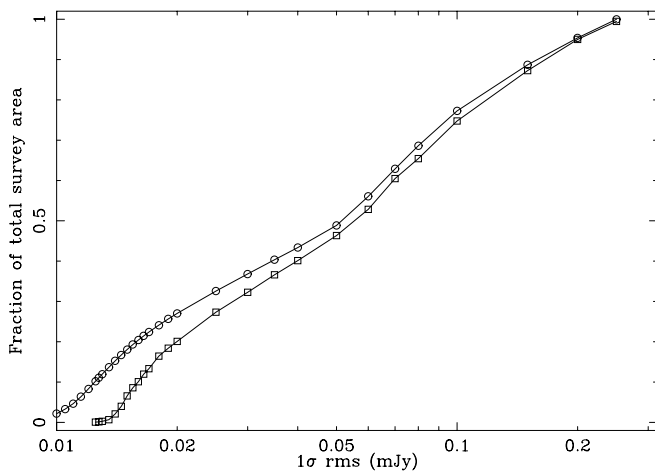


FIG. 9.—Fraction of the survey area having an rms noise level equal to or lower than the flux densities indicated, used in constructing the weighting corrections for the source counts. The circles represent the areas derived from the theoretical noise level image for the mosaic; the squares give the actual measured values.

normalization was made (Ryle 1968; Longair 1966). It has persisted in the literature of radio source-count investigations and is similarly used here for ease of comparison with other surveys. We do not, however, normalize by the additional factor of 225 that is sometimes used to fix the value of the differential source count to unity at a flux density of 1 Jy.

6. RESULTS

The differential source counts were calculated for both the primary PDF catalog and the deep independent catalog, and the results are presented in Tables 3 and 4 and are shown in Figure 10. Tables 3 and 4 give the flux density extrema and the mean flux density of each bin, the actual number of sources in each bin (N), and the effective number of sources (N_{eff}) over the whole 4.56 deg^2 area after applying the weighting and resolution corrections, along with the resulting source counts. The mean flux density in each bin was calculated from the flux densities of the detected sources in each bin, except toward the brighter flux densities where the formula given by Windhorst et al. (1984, their eq. [19]) was used, making use of the known slope of the source counts to more accurately estimate the mean flux density in a bin. This is especially important for the brightest bin from each catalog, where fewer objects are available to accurately represent the mean flux density of a bin. Figure 10 indicates the flux density range for each bin by a horizontal bar, while the vertical uncertainties are the statistical uncertainties in the counts, described above. The primary and deep PDF catalogs allow the source counts constructed from the PDF to span a flux density range from about 0.05–100 mJy, although the sampling becomes sparse at brighter flux densities. This reflects the limited area of the survey, which sharply restricts the number of sources detectable at brighter flux densities. In the counts from the deep independent catalog, covering a smaller area still, this effect is seen to appear at lower flux densities.

Given that the resolution and weighting corrections have been carefully applied, the drop off in the source counts seen toward the faintest flux densities should not immediately be discounted as incompleteness in the counts. Also, since the faintest few source-count bins may be biased high by the presence of falsely detected sources, it is possible that the observed drop off may be even greater. The angular size distribution from which the resolution correction is derived, however, has larger uncertainties at these lower flux densities, which could be compounded by the actual incompleteness present in the source catalogs. This may have the effect of producing the observed drop off in the measured

TABLE 3
SOURCE COUNTS FROM THE DEEPEST PDF REGION

Range in $S_{1.4}$ (mJy)	$\langle S_{1.4} \rangle$ (mJy)	N	N_{eff}	$(dN/dS)/S^{-2.5}$ ($\text{Jy}^{1.5} \text{sr}^{-1}$)
0.048–0.067.....	0.057	64	149.9	2.49 ± 0.49
0.067–0.078.....	0.072	64	75.2	3.27 ± 0.41
0.078–0.095.....	0.086	66	86.0	3.66 ± 0.58
0.095–0.115.....	0.104	63	70.0	4.00 ± 0.50
0.115–0.150.....	0.131	61	65.8	3.99 ± 0.51
0.150–0.202.....	0.174	60	63.6	5.04 ± 0.65
0.202–0.409.....	0.288	60	62.7	4.56 ± 0.59
0.409–18.2.....	2.75	53	54.8	13.04 ± 1.79

TABLE 4
SOURCE COUNTS FROM THE PRIMARY PDF CATALOG

Range in $S_{1.4}$ (mJy)	$\langle S_{1.4} \rangle$ (mJy)	N	N_{eff}	$(dN/dS)/S^{-2.5}$ ($\text{Jy}^{1.5} \text{sr}^{-1}$)
0.089–0.111.....	0.100	159	1172.2	3.91 ± 1.25
0.111–0.133.....	0.122	157	804.7	4.25 ± 0.90
0.133–0.159.....	0.146	154	606.9	4.44 ± 0.41
0.159–0.186.....	0.172	157	492.8	4.96 ± 0.48
0.186–0.227.....	0.206	157	437.4	4.73 ± 0.39
0.227–0.282.....	0.253	150	353.7	4.67 ± 0.39
0.282–0.376.....	0.326	155	297.9	4.37 ± 0.36
0.376–0.531.....	0.447	151	236.6	4.64 ± 0.39
0.531–0.759.....	0.635	150	191.5	6.15 ± 0.52
0.759–1.18.....	0.945	150	168.2	7.98 ± 0.66
1.18–2.32.....	1.65	153	164.7	11.50 ± 0.94
2.32–10.5.....	4.91	152	160.8	23.98 ± 1.96
10.5–115.....	33.3	57	60.0	84.39 ± 11.18

source counts at these low flux densities. This bias would be in the opposite direction to that expected from the presence of falsely detected sources. In addition, the source counts are eventually expected to converge below a few microjanskys in order for their integrated sky brightness not to distort the observed cosmic background radiation spectrum at centimeter wavelengths (Windhorst et al. 1993). Although it is unlikely that this effect is occurring at the flux densities probed here, the observed source counts may be starting to give an indication of a new slope change at levels around 50–100 μJy (but cf. Richards 2000).

Figure 11 shows the newly derived PDF source counts and adds other source-count estimates from existing surveys for comparison. The compilation of source counts from Windhorst et al. (1993) is shown, as well as those from the Faint Images of the Radio Sky at Twenty cm survey (FIRST, White et al. 1997), the counts from the Very Large Array (VLA) observations of the Hubble Deep Field (HDF, Richards 2000), and those of Prandoni et al. (2001). A previous estimate of the source counts from an earlier ATCA mosaic of the Phoenix region (Hopkins et al. 1999b) is also

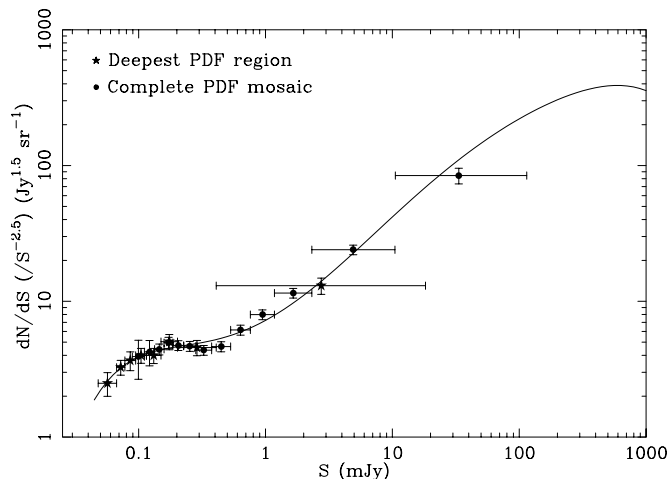


FIG. 10.—1.4 GHz differential source counts for the deep independent $33' \times 33'$ region within the PDF (stars) and the primary catalog (circles). Horizontal uncertainties represent the flux density range of each source-count bin. The line is a sixth-order polynomial fit described in the text.

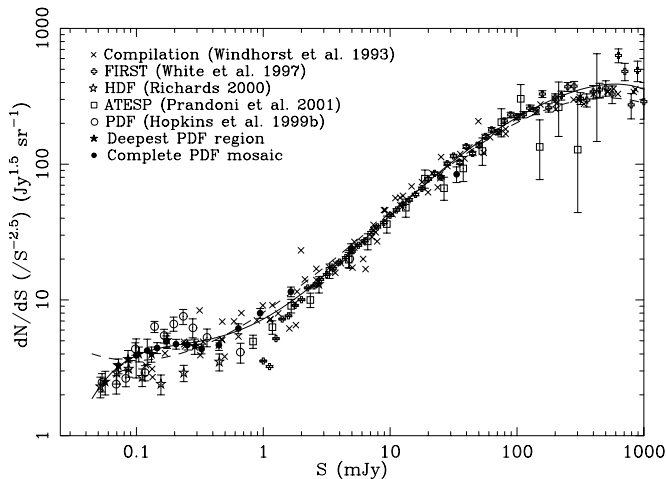


FIG. 11.—1.4 GHz differential source counts for the primary PDF catalog (*filled circles*) and deep independent catalog (*filled stars*). For comparison we also show the compilation of source counts from Windhorst et al. (1993), source counts from the FIRST survey (White et al. 1997), those from the ATESP survey (Prandoni et al. 2001), and from VLA observations of the HDF (Richards 2000). Previously estimated source counts from an earlier ATCA mosaic of the Phoenix area are also shown (Hopkins et al. 1999b). The solid line is a sixth-order least-squares polynomial fit. The third-order polynomial fit from Katgert et al. (1988) is also shown for comparison (*dashed line*).

shown for comparison. The similarities and discrepancies between these various results are discussed in § 7.

The solid line in both Figures 10 and 11 is a linear least-squares sixth-order polynomial fit, derived in order to aid other workers in this field. The fit was constructed using the newly derived PDF counts from both the deep and primary catalogs. Given the sparsity of our sampling of the source counts above about 2 mJy and our consistency with the counts from FIRST in that regime, we supplement our counts with the FIRST source-count values above 2.5 mJy, where they are complete. We also excluded the brightest PDF source-count bin from the fit since, although its uncertainties indicate it is consistent with the counts from FIRST, it clearly lies lower than those counts and if retained would bias the resulting fit somewhat. The resulting polynomial fit is given by

$$\log[(dN/dS)/(S^{-2.5})] = \sum_{i=0}^6 a_i [\log(S/\text{mJy})]^i, \quad (8)$$

with $a_0 = 0.859$, $a_1 = 0.508$, $a_2 = 0.376$, $a_3 = -0.049$, $a_4 = -0.121$, $a_5 = 0.057$, and $a_6 = -0.008$. This fit is valid over the flux density range 0.05–1000 mJy. A previously published fit to the source counts down to about 100 μJy was of a third-order polynomial by Katgert, Oort, & Windhorst (1988), also shown in Figure 11 for comparison. Our sixth-order polynomial is substantially similar to this third-order one above 100 μJy . A higher order polynomial is necessary to account for both the number of changes of slope in the observed counts, as well as the sense of the curvature below 100 μJy . A fourth-order polynomial would be sufficient to model these features, but it was found that, in this case, the point of inflection around 0.5 mJy was poorly represented. To ensure that the polynomial showed concave down curvatures at the extremes, a sixth-order polynomial was thus required. The residuals from the sixth-order fit

above have an rms of about 0.04 in the logarithm of the normalized counts.

7. DISCUSSION

While it is clear that there is a high level of consistency between most source-count estimates over a broad range of flux densities and the PDF source counts are consistent with the compilation of source counts given by Windhorst et al. (1993) down to about 150 μJy , there are discrepancies that warrant attention. These are primarily the apparent inconsistency with earlier PDF counts (Hopkins et al. 1999b), the discrepancy around 1 mJy between several catalogs, and the discrepancy with the deep VLA counts of the HDF (Richards 2000). We explore these discrepancies here.

We have established that the earlier PDF source-count estimate suffers from the artifact due to overestimates of source extent, and hence integrated flux density, for objects detected near the threshold of the survey as described in § 5 above. This results in an overestimate in the counts from about 150–300 μJy and an underestimate below about 100 μJy . Also, the strong variation from point to point in these counts is attributable to the relatively low minimum number of objects (30) per bin used in generating those counts. When these issues are addressed the counts derived from that earlier catalog are seen to be identical with the current estimate over the full flux density range probed.

At flux densities below about 2 mJy the source counts from FIRST systematically drop away from the compilation of counts from Windhorst et al. (1993). This is described by White et al. (1997) as due to the low peak flux densities of many faint extended sources undetectable in the FIRST survey, and this feature is thus an indicator of the incompleteness of the survey at its faint limit. As mentioned above, in determining the polynomial fit, we have used only FIRST source-count points from flux density bins brighter than 2.5 mJy to avoid these incomplete bins.

The source counts from the Australia Telescope ESO Slice Project (ATESP) survey (Prandoni et al. 2001) around 1 mJy are also lower than the PDF counts and the source-count compilation. The ATESP survey covers a large area (26 deg²) with a fairly uniform rms noise level (fluctuating between about 70–100 μJy) and detects sources down to about 0.5 mJy (Prandoni et al. 2000a, 2000b). The discrepancy is seen in the two ATESP bins spanning 0.7–1.4 mJy, so the inconsistency between these counts and those from the PDF occurs at a relatively high S/N level ($\sim 10\sigma$). Recognizing that great effort has been spent in ensuring that the catalogs and source counts for both ATESP and the PDF are as reliable as possible, we have explored this issue in some detail in an attempt to reconcile the two. Using the publicly available ATESP catalog and the primary PDF catalog we have directly compared actual source surface densities, and we find that the difference is present in the catalogs, rather than being an artifact of the construction of the source counts. The surface density of sources between the catalogs was found to differ by the same fraction as the source counts.

The ATESP team have already established that field-to-field variance resulting from galaxy clustering could account for perhaps roughly half this discrepancy. They constructed source counts for independent regions within their large survey area to explore the extent of the fluctuations seen. From the angular correlation functions of Georgakakis

et al. (2000) and Windhorst, Mathis, & Neuschaefer (1990), such effects are likely to be on the order of 10%–20% of the measured source counts, and this is consistent with the level of variation seen within the ATESP study. This is not sufficient to account for the full discrepancy seen around 1 mJy. We then explored differences between the source detection procedures used (ATESP uses the task IMSAD in MIRIAD for source detection). By using SFIND to measure sources in several of the individual ATESP mosaics, we established the following results. The SFIND and IMSAD measurements are highly consistent, within expected Gaussian fitting uncertainties, for the majority of sources. At very low S/N there are some inconsistencies between the two tasks in the measurements for a small fraction of sources, related to the selection of pixels for inclusion in the Gaussian fitting, but even for these objects the measured integrated flux densities are mostly consistent. The surface densities of the SFIND catalogs for the ATESP mosaics are consistent with that of the PDF catalog, although in the range of the discrepancy the PDF catalog is at the upper end of the observed field-to-field variations between the ATESP mosaics. The main difference between the IMSAD and SFIND catalogs in the ATESP mosaics appears to be explained by complex sources split into components during the fitting procedure by both tasks. The ATESP survey has examined and refit such complex sources individually to construct a “source catalog” rather than a “component catalog,” whereas the present investigation for the Phoenix survey neglects this step for reasons given in § 4 above. When the ATESP source counts are constructed using the component catalog the source-count value is increased by about 10% in the flux density region of the discrepancy (I. Prandoni 2002, private communication).

From these results we conclude that the discrepancy between the ATESP and PDF source counts is attributable to two main effects. First, calculating the source counts based on a component catalog rather than a source catalog increases the resulting source count by about 10%. This combined with a field to field variation putting the PDF counts to the higher end of observed variations in this flux density range, consistent with expected variations from measurements of the angular correlation function, is sufficient to account for the observed discrepancy.

The deep VLA source counts of the HDF region, compiled by Richards (2000), also show a discrepancy with the PDF source counts and those in the source-count compilation. Above about 100 μ Jy the HDF counts deviate by up to a factor of 2 below the counts of other surveys. This discrepancy has already been described in detail by Richards (2000), and we can add little to that discussion other than the comment that the extent of this deviation again seems to be larger than can be explained through the expected fluctuations from galaxy clustering (Georgakakis et al. 2000; Windhorst et al. 1990).

Apart from these discrepancies, the 1.4 GHz source counts seem now to be consistently determined from the brightest levels down to about 50 μ Jy. The sixth-order polynomial fit to the counts given here will provide a useful parametrization of the counts above this level.

8. SUMMARY

We have used the ATCA to construct a 1.4 GHz mosaic image of slightly more than 4.5 deg². This image reaches rms noise levels of about 12 μ Jy at its most sensitive, and a primary catalog of 2058 radio sources in the mosaic has been constructed with a 10% false discovery rate. Detailed analysis of the source measurement in independently observed pointings confirm the reliability of the cataloged source parameters, consistent with the expected uncertainties from the image noise and the Gaussian source fitting. Differential source counts were constructed for both a deep independent catalog of a 33' \times 33' region centered on the most sensitive portion of the survey, and the full primary PDF catalog. The source counts are seen to be consistent with previous surveys of similar size, while sampling to fainter flux densities, and sensitivity, while sampling a larger area. Discrepancies between the ATESP source counts and those of the PDF at levels of 1 mJy have been explored in detail. These are attributable to a field-to-field variation increasing the PDF counts slightly over the flux density range of the discrepancy and are otherwise consistent with the source counts derived from the ATESP component catalog. We have performed a sixth-order polynomial fit to our derived source counts, supplemented at the bright end by those from FIRST, which adequately parametrizes the source counts from 0.05–1000 mJy. The 1.4 GHz radio mosaic and catalogs are available on the World Wide Web at <http://www.atnf.csiro.au/~ahopkins/phoenix>, or from the authors by request.

The authors would like to thank the referee for several very helpful suggestions and extend their warmest thanks to Isabella Prandoni for helpful discussions and for kindly making several of the ATESP mosaics available for analysis. A. M. H. gratefully acknowledges support provided by NASA through Hubble Fellowship grant HST-HF-01140.01-A awarded by the Space Telescope Science Institute, which is operated by the Association of Universities for Research in Astronomy, Inc., for NASA, under contract NAS 5-26555. J. A. gratefully acknowledges the support from the Science and Technology Foundation (FCT, Portugal) through the fellowship BPD-5535-2001 and the research grant ESO-FNU-43805-2001. The Australia Telescope is funded by the Commonwealth of Australia for operation as a National Facility managed by CSIRO.

REFERENCES

- Afonso, J. M. 2002, Ph.D. thesis, Univ. London
 Afonso, J., Mobasher, B., Chan, B., & Cram, L. 2001a, *ApJ*, 559, L101
 Afonso, J., Mobasher, B., Georgakakis, A., Cram, L., & Hopkins, A. 2001b, *ApSS*, 277, 527
 Afonso, J., Mobasher, B., Hopkins, A. M., & Cram, L. 2001c, *Ap&SS*, 276, 941
 ———. 1999, in *Building Galaxies: from the Primordial Universe to the Present*, ed. F. Hammer et al. (Gif-sur-Yvette: Ed. Frontières)
 Condon, J. J. 1997, *PASP*, 109, 166
 Condon, J. J., Condon, M. A., & Hazard, C. 1982, *AJ*, 87, 739
 de Vries, W. H., Morganti, R., Röttgering, H. J. A., Vermeulen, R., van Breugel, W., Rengelink, R., & Jarvis, M. J. 2002, *AJ*, 123, 1784
 Georgakakis, A. 1999, Ph.D. thesis, Univ. London
 Georgakakis, A., Mobasher, B., Cram, L., Hopkins, A., Lidman, C., & Rowan-Robinson, M. 1999a, *MNRAS*, 306, 708
 Georgakakis, A. E., Mobasher, B., Cram, L., & Hopkins, A. 1999b, *MNRAS*, 310, L15
 Georgakakis, A., Mobasher, B., Cram, L., Hopkins, A., & Rowan-Robinson, M. 2000, *A&AS*, 141, 89
 Hopkins, A. M. 1998, Ph.D. thesis, Univ. Sydney

- Hopkins, A., Cram, L., Mobasher, B., & Georgakakis, A. 1999a, in *Looking Deep in the Southern Sky*, ed. R. Morganti & W. J. Couch (New York: Springer), 120
- Hopkins, A., Afonso, J., Cram, L., & Mobasher, B. 1999b, *ApJ*, 519, L59
- Hopkins, A., Georgakakis, A., Cram, L., Afonso, J., & Mobasher, B. 2000, *ApJS*, 128, 469
- Hopkins, A. M., Miller, C. J., Connolly, A. J., Genovese, C., Nichol, R. C., & Wasserman, L. 2002, *AJ*, 123, 1086
- Hopkins, A. M., Mobasher, B., Cram, L., & Rowan-Robinson, M. 1998, *MNRAS*, 296, 839
- Katgert, P., Katgert-Merkelijn, J. K., Le Poole, R. S., & van der Laan, H. 1973, *A&A*, 23, 171
- Katgert, P., Oort, M. J. A., & Windhorst, R. A. 1988, *A&A*, 195, 21
- Longair, M. S. 1966, *MNRAS*, 133, 421
- Masci, F. J., et al. 2001, *PASP*, 113, 10
- Miller, C. J., et al. 2001, *AJ*, 122, 3492
- Mobasher, B., Afonso, J., & Cram, L. 2001, in *Deep Fields*, ed. S. Cristiani, A. Renzini, & R. E. Williams (New York: Springer), 144
- Mobasher, B., Cram, L., Georgakakis, A., & Hopkins, A. M. 1999, *MNRAS*, 308, 45
- Oosterbaan, C. E. 1978, *A&A*, 69, 235
- Prandoni, I., Gregorini, L., Parma, P., de Ruiter, H. R., Vettolani, G., Wieringa, M. H., & Ekers, R. D. 2000a, *A&AS*, 146, 31
- . 2000b, *A&AS*, 146, 41
- . 2001, *A&A*, 365, 392
- Rengelink, R. B., Tang, Y., de Bruyn, A. G., Miley, G. K., Bremer, M. N., Röttgering, H. J. A., & Bremer, M. A. R. 1997, *A&AS*, 124, 259
- Richards, E. A. 2000, *ApJ*, 533, 611
- Richards, E. A., Kellermann, K. I., Fomalont, E. B., Windhorst, R. A., & Partridge, R. B. 1998, *AJ*, 116, 1039
- Ryle, M. 1968, *ARA&A*, 6, 249
- Sadler, E. M., et al. 2002, *MNRAS*, 329, 227
- White, R. L., Becker, R. H., Helfand, D. J., & Gregg, M. D. 1997, *ApJ*, 475, 479
- Windhorst, R. A., Fomalont, E. B., Partridge, R. B., & Lowenthal, J. D. 1993, *ApJ*, 405, 498
- Windhorst, R. A., Mathis, D., & Neuschaefer, L. 1990, in *ASP Conf. Ser. 10, Evolution of the Universe of Galaxies* (San Francisco: ASP), 389
- Windhorst, R. A., van Heerde, G. M., & Katgert, P. 1984, *A&AS*, 58, 1